CLINICAL ELECTRON BEAM DOSIMETRY: BASIC DOSIMETRY DATA

Kenneth R. Hogstrom
Department of Radiation Physics
The University of Texas M. D. Anderson Cancer Center
Houston, TX 77030

INTRODUCTION

Clinical electron beam dosimetry implies a study of all phases of the measurement and calculation of dose necessary for electron-beam therapy. This paper will cover a selected portion of that knowledge, primarily dealing with the dose to a water phantom. It is the goal of this paper not only to demonstrate the dependence of dose on electron beam parameters, but to provide a qualitative explanation of that dependence on the physical nature of the electron-beam interaction.

First, there is a discussion of the fundamental physical principles of electron interactions (multiple Coulomb scattering and stopping power) and how they influence the dose distribution (depth dose, output, and isodose curves). Second, the basic dosimetry data utilized for patient dosimetry are discussed. This includes depth dose, output factors, and isodose curves, both at standard and extended SSD. Third, beam modifiers often used with electrons (blocking and bolus) are introduced. Last, the clinical specifications for dose prescription and for a single electron beam are discussed. Treatment and treatment planning techniques, the effect of the patient on the dose distribution, and computer algorithms for dose calculations are not discussed.

The knowledge presented in this work is based on methods currently in clinical practice at the The University of Texas M. D. Anderson Cancer Center. These methods are, for the most part, consistent with the material presented by ICRU (1984) and the AAPM (1983) Task Group 21 calibration protocol. They are also consistent with the recommendations of AAPM Task Group 25 (Khan et al., 1991), which was charged with developing a set of recommendations for clinical electron-beam dosimetry consistent with the previous two documents.

PHYSICAL PRINCIPLES

To understand the dependence of electron-beam dose distributions on various beam parameters and the patient, it helps to have an understanding of the fundamental principles of electron interactions. Three basic interactions are significant for electron transport at energies used in electron-beam radiation therapy (1-25 MeV): collisional energy loss, bremsstrahlung energy loss, and multiple Coulomb scattering (MCS). ICRU (1984) discusses these principles in some detail; the aim of this section is to relate those principles to measured beam dosimetric data.

Figure 1 illustrates electron transport in matter; two dominating features are observed in the electron tracks, the finite range due to stopping power and the increase in lateral spread with depth due to multiple Coulomb scattering.

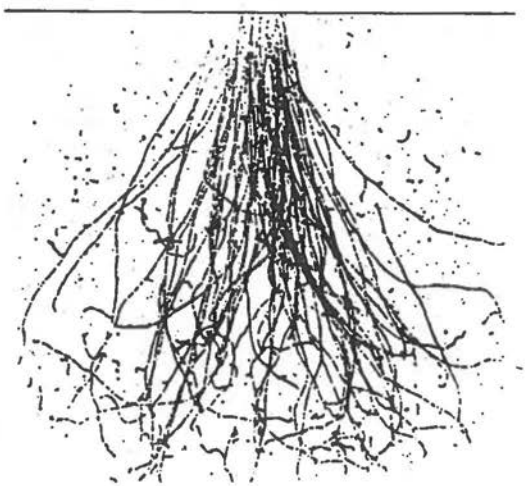

Figure 1. Bubble chamber photograph of a 9.3-MeV electron pencil beam propagating through propane.

A. Depth-dose Curve

By constructing the depth-dose curve piecemeal, we can appreciate the role of the basic physical interactions on dose. Consider a broad parallel electron beam normally incident on a semi-infinite water phantom, where z is the depth below its surface. If the electron beam were to experience only collisional energy loss with other electrons, and delta ray production were ignored, then the depth-dose curve labeled 1 in Fig. 2(b) would be observed. Dose, the product of fluence, Φ, and mass stopping power is given by

$$D(z) = \int_E \Phi_E(z) \frac{S_E}{\rho} \, dE \quad , \tag{1}$$

where Φ_E is the fluence weighted energy spectrum at depth z and S_E/ρ is the mass stopping power for electrons of energy E. Because there is no scatter, all electrons lose energy at the same rate with depth so that D(z) is given by

$$D(z) = \Phi_0 \, [S(z)/\rho] \quad , \tag{2}$$

where Φ_0 is constant from the surface to the continuous slowing down approximation (CSDA) range, r_0, and zero thereafter (cf. curve 1 of Fig. 2(a)). Collision stopping power from 1-25 MeV is 2.0±0.2 MeV $g^{-1}cm^2$, so

that a range in cm of approximately one-half the energy in MeV is observed. Also, the nearly constant stopping power results in a reasonably constant depth dose; only near the end of the range (E<1 MeV) does the collision stopping power begin increasing approximately as E^{-2}, resulting in the sharp increase in dose in Fig. 2(b).

The influence of multiple Coulomb scatter is two fold. First, it forces the electrons along winding paths (cf. Fig. 1), so that the penetration of electrons with depth below the surface varies, resulting in range straggling. The resulting effect on the electron fluence is illustrated in Fig. 2(a) (curve 2). Second, MCS explains the slow buildup of depth dose. As the electrons become angulated with respect to their incident direction, their range decreases so that all of their energy is lost to the water at a shallower depth, resulting in an increased dose. Another way of looking at this phenomenon is that the electrons become angulated with depth. As

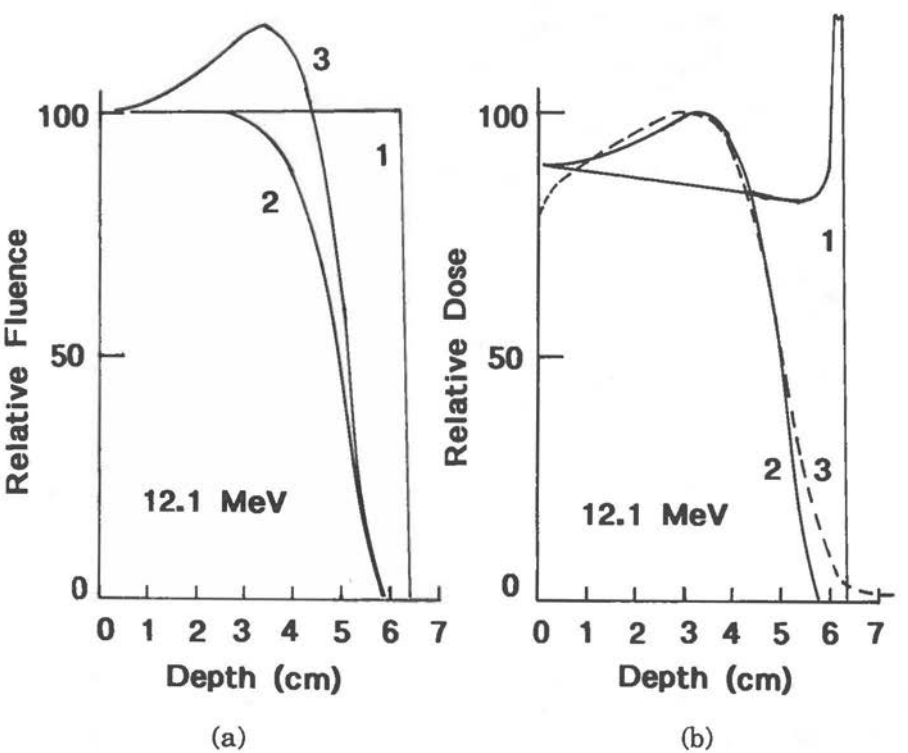

Figure 2. (a) Fluence versus depth in water is calculated for a 12.1 MeV electron beam. Curve 1 represents the fluence (or planar fluence) calculated assuming no scatter and the CSDA approximation for energy loss. After MCS is introduced, Curve 2 is the planar fluence and Curve 3 the fluence. (b) Depth dose in water is calculated for a 12.1 MeV beam. Curve 1 represents the dose calculated assuming no scatter and the CSDA approximation for energy loss. The depth dose including MCS, shown as Curve 2, is similar in shape to the depth dose (Curve 3) measured for the 13-MeV beam ($E_{p,o}$=12.1 MeV) on the Therac 20.

illustrated in Fig. 3, angulation of the electrons increases the fluence by $(\cos \theta)^{-1}$ and hence increases the dose. As the electrons lose energy, their scattering power increases, so that the mean angulation of the electron beam increases with depth. This results in a slow buildup of dose (Boag, 1972), with the rate of buildup being more for the lower energy electron beams as scattering power is inversely proportional to energy. Electrons scattered through large angles will "range out" sooner so that at about half the range the angular distribution's increase stops. The resulting fluence and depth-dose distribution is illustrated in Fig. 2(a) (curve 3) and Fig. 2(b) (curve 2), respectively. In short, the decrease in dose distally due to range straggling is taken up by the increase in dose at shallow depths due to fluence buildup so that total energy deposition is conserved.

In Fig. 2(b), the measured depth-dose curve (curve 3) for the 13-MeV ($E_{p,o}$ =12.1 MeV) beam of the Therac 20 is plotted for comparison to that calculated (curve 2) assuming only CSDA energy loss and MCS, based on ICRU (1984) collision stopping powers and angular scattering powers of water, respectively. The close similarities in the shapes of the measured and calculated depth-dose curves demonstrate the significances of these two physical processes in the dosimetry of therapeutic electron beams. The difference in the first centimeter is attributed to the buildup of secondary electrons (Andreo and Brahme, 1983) from delta-ray production. The bremsstrahlung component of the dose, primarily arising from the accelerator end window, accounts for differences in the buildup region, but is seen mostly at depths beyond the practical range. Differences in the falloff region are due to the stochastic nature of electron energy loss.

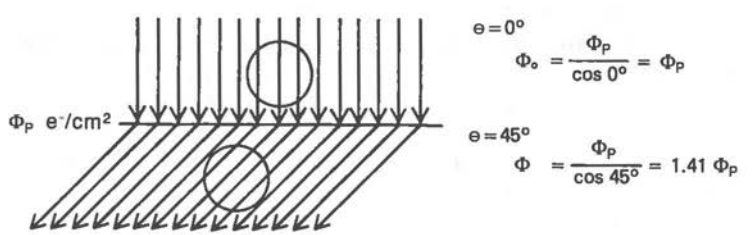

Figure 3. The angulation of electrons relative to the incident beam direction results in an increase in fluence. This example illustrates how a 45° angulation leads to a 41% increase in fluence (from Hogstrom and Almond, 1982).

B. Side-scatter Equilibrium

For finite field sizes, a dependence of depth-dose and output on field size is observed owing to the multiple Coulomb scatter in both the patient and in air. To understand this dependence, an understanding of the

impact of lateral deflections resulting from multiple Coulomb scattering is achieved by introducing the concept of side-scatter equilibrium.

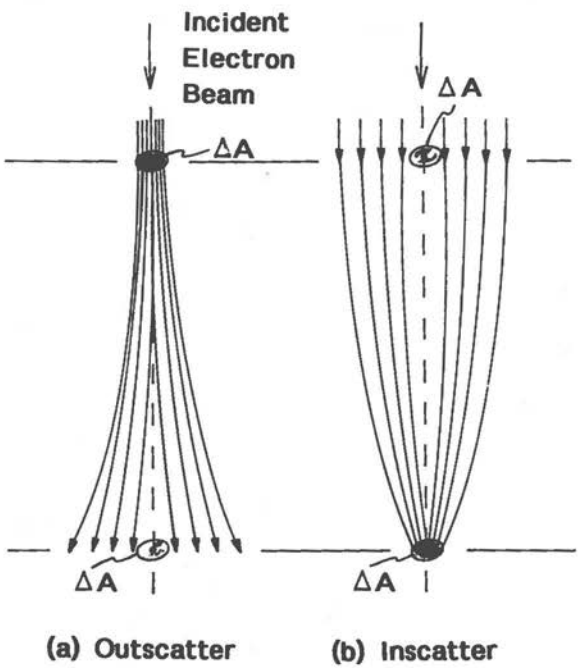

Figure 4. Concept of side-scatter equilibrium: (a) Electrons passing through an area ΔA upstream undergo scatter so that they miss the target area ΔA below. (b) For each electron that scatters away from ΔA, there is an electron incident outside ΔA that scatters into ΔA following a similar path. If the electron beam is broad enough so that in-scattered electrons equal out-scattered electrons in a small area (ΔA) about a point, then side-scatter equilibrium is said to hold at that point.

The concept of side-scatter equilibrium is important in electron beam dosimetry, as is the concept of equilibrium of secondary scattered electrons in the dose buildup of x-ray beams. The principle of side-scatter equilibrium is defined in Fig. 4. This principle can now be applied to various measurement conditions, as illustrated qualitatively in Fig. 5. Any electron passing through the final beam-defining collimator has a probability of reaching a particular point in the phantom. The probability is a function of (1) the location of the electron as it passes through the collimator, (2) the angular distribution of the electrons at that point, and (3) the probability that the particle will be scattered such that it will arrive at the point of interest. In Fig. 5(a), it is seen that the spatial distribution of electrons at the collimator, which reach a point at the depth of maximum dose on central axis, is approximately Gaussian in shape. If most all electrons (e.g. >99%) reach the point of interest, then side-scatter equilibrium is said to exist. Such is the case for the reference geometry in Fig. 5(a).

If the collimator closes sufficiently, then some electrons that could have reached the point of interest (R_{100}) are removed from the beam (Fig. 5(b)). In this case, side-scatter equilibrium does not exist, and a decrease in the output factor is observed with decreasing field size.

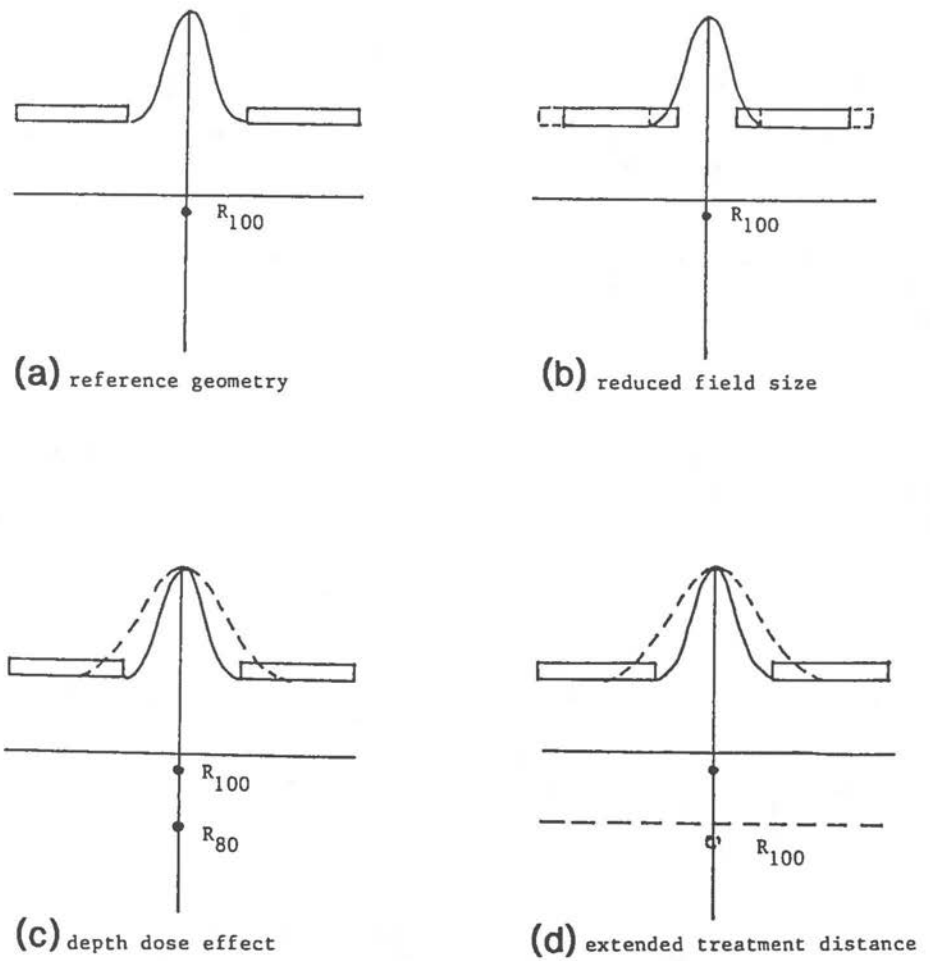

Figure 5. These figures show the probability distribution for an electron at the level of the collimator reaching a point at depth on central axis. This is due to both the scattering of electrons in air and in phantom. (a) For the depth of maximum dose, R_{100}, the field size is large enough so that all the electrons that could, reach R_{100}; (b) the field size is reduced from that of the reference geometry, indicated by dashed collimators, resulting in some electrons striking the collimator and not reaching R_{100}, and hence a dose reduction; (c) indicated by the dashed curve is the electron distribution that would reach R_{80} due to additional phantom scatter were the collimator opened sufficiently; (d) indicated by the dashed curve is the distribution of electrons that would reach R_{100} with the water surface at an extended air gap, were the collimator opened sufficiently.

In Fig. 5(c), the spatial distribution of electrons reaching a point at a deeper depth (R_{80}) is seen to be broader than that for the point at R_{100}. This is primarily due to multiple Coulomb scattering in the phantom. As the collimator closes, the point at the deeper depth is influenced first, losing side-scatter equilibrium, which results in a decreased percentage depth dose, hence explaining the field-size dependence of depth dose.

In Fig. 5(d), the spatial distribution of electrons reaching the depth of maximum dose (R_{100}) for an extended treatment distance is compared with that of Fig. 5(a). This explains the major reason for the output decreasing faster than inverse square for small fields at extended treatment distances.

It should be understood that once a point begins losing side-scatter equilibrium, it can be considered to lie in the penumbra of the field. Therefore, one should be extremely careful in understanding the dose distribution for small field sizes or extended treatment distances. This effect is most significant at low electron energies, since the angular scattering power for electrons is approximately inversely proportional with the square of the energy.

BASIC DOSIMETRY DATA

The purpose of this section is to discuss basic dosimetry data utilized for patient dosimetry. The dependence of depth dose, output, and isodose curves in water on electron beam energy, field size, and air gap are discussed. The various methods of dose measurement for these data are not discussed here; the reader is referred to AAPM TG-25 Report (Khan et al., 1991) for AAPM recommendations.

A. Depth Dose

The depth-dose curve is important for the selection of the appropriate electron beam energy which should cover the target volume at its maximum depth while adequately sparing the deeper critical structures. Properties of the electron beam depth-dose curve are illustrated in Fig. 6. The surface dose, D_s, is defined at 0.05 cm. A high D_s is desirable if skin and subcutaneous tissues are included in the target volume; a low D_s is desirable if the skin is meant to be spared. Because of the flatness of the depth-dose curve in the neighborhood of R_{100}, the depth of dose maximum, R_{100}, can vary significantly with machine and field size for a particular energy and has little clinical significance in electron-beam dosimetry. The depth of dose maximum depends strongly upon design of the machine head (Bruinvis et al., 1985), particularly in how it affects the amount of scatter off secondary collimators. The therapeutic depth is typically selected as the depth of the 90% dose, R_{90}. This depth is important in that it should normally exceed the maximum depth of the target volume. A good rule-of-thumb is that R_{80} in cm approximately equals one-third of the most

probable incident energy, $E_{p,o}$, in MeV. For example, to treat to a depth of 4 cm, an energy of at least 12 MeV is necessary, as it is recommended to treat to R_{90}, which is slightly less than R_{80}. The practical range, R_p, is important in that critical structures distal to that value are typically spared any significant radiation dose. A good rule-of-thumb is that R_p in cm approximately equals one-half of the most probable incident energy in MeV. The distance between R_p and R_{90} is a measure of the sharpness of dose falloff and is a measure of the minimum distance between the distal tumor and the critical structure for which the critical structure can be spared. In ICRU 35 the sharpness of dose falloff is characterized by the quantity G_o, defined in Fig. 6. The bremsstrahlung dose, D_x, is usually most significant in arc electron therapy, where the bremsstrahlung dose is focused in the vicinity of isocenter (Hogstrom and Leavitt, 1987).

Properties of the depth-dose curve are a strong function of machine design and beam energy. Figure 7 illustrates a set of depth-dose curves for various energies on a typical linear accelerator. The following properties are observed: (1) surface dose increases with increasing energy, (2) the therapeutic treatment depth linearly increases with energy, and (3) the bremsstrahlung dose increases with energy. The machine dependence of these three quantities is illustrated in Figs. 8-10. In Fig. 8, a non-linear increase of surface dose with energy from 6 to 20 MeV is observed. In general, we see that the Therac 20, a scanned beam with trimmer bar collimation, produces the lowest surface doses. The Mevatrons, which utilize a dual-scattering foil system and little collimator scatter, show slightly higher surface doses. Finally, the Clinacs, which utilize a dual scattering foil system as well as scatter off the collimators to flatten the beam, have the highest surface doses. Therefore, one can conclude that the addition of secondary, low-energy electrons from scattering foils and from collimator scatter tend to increase the surface dose. In Fig. 9, each machine's R_{90} as a function of energy is compared. The Therac 20, having the most monoenergetic incident energy spectra, results in the greatest R_{90} as a function of energy. This is most evident at the higher energies, where the thicker scattering foils tend to degrade the energy spectrum. The increased R_{90} of the Clinacs relative to the Mevatrons is a reflection of the former's thinner scattering foils. In Fig. 10, each machine's bremsstrahlung dose as a function of energy is compared. The Therac 20, a scanned beam, has the lowest bremsstrahlung doses. The Clinacs have lower bremsstrahlung doses compared with the Mevatrons, as they have thinner primary scattering foils.

In summary, the scanned electron beams indicate more clinical utility for higher electron energies, as they have the most penetration, sharpest dose falloff (R_{90}-R_{10}), and least bremsstrahlung dose. The Clinacs' depth-dose properties appear more favorable than those of the Mevatrons in that they tend to have a higher surface dose, deeper therapeutic depth, and decreased bremsstrahlung. Although the thinner scattering foils of the Clinacs produce a better quality depth dose, they do not produce as flat of a

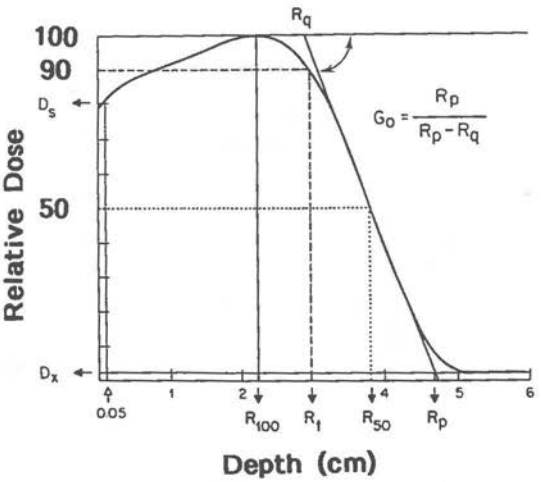

Figure 6. Properties of a typical electron beam depth-dose curve are defined. The therapeutic depth is recommended to be R_{90} (from Khan, et al., 1991).

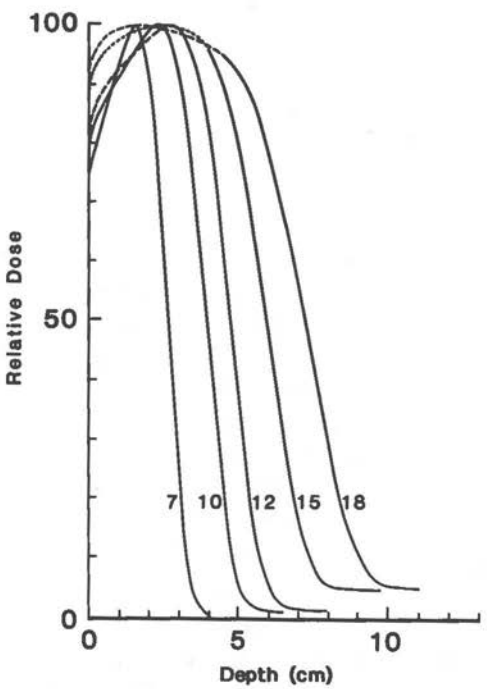

Figure 7. Comparison of large field (10x10 cm) depth-dose curves for different nominal energies on a Mevatron 77 (from Meyer et al., 1984).

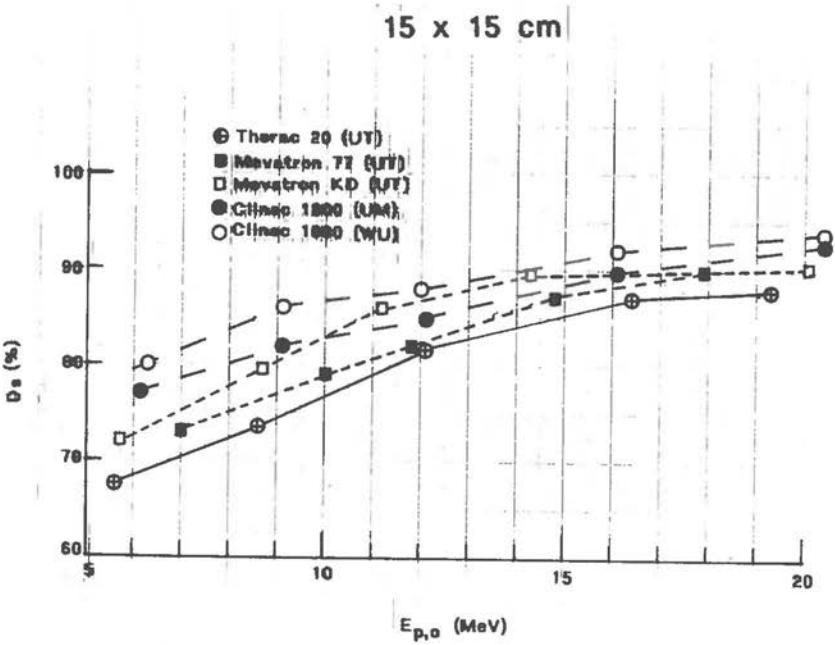

Figure 8. Comparison of surface dose versus electron energy for all energies of the Therac 20, Mevatron, and Clinac radiotherapy accelerators (from NCI Working Group, 1989).

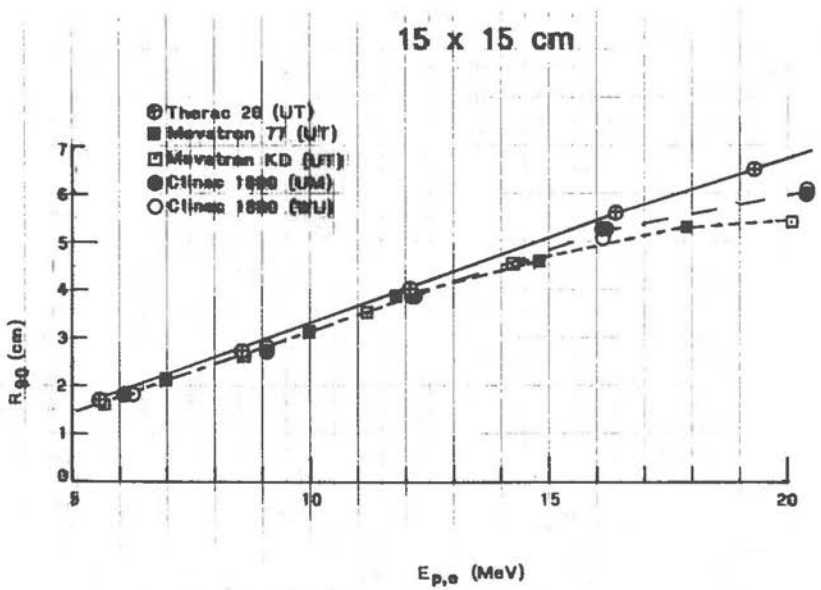

Figure 9. Comparison of therapeutic depth, R_{90}, versus electron energy for all energies of the Therac 20, Mevatron, and Clinac radiotherapy accelerators (from NCI Working Group, 1989).

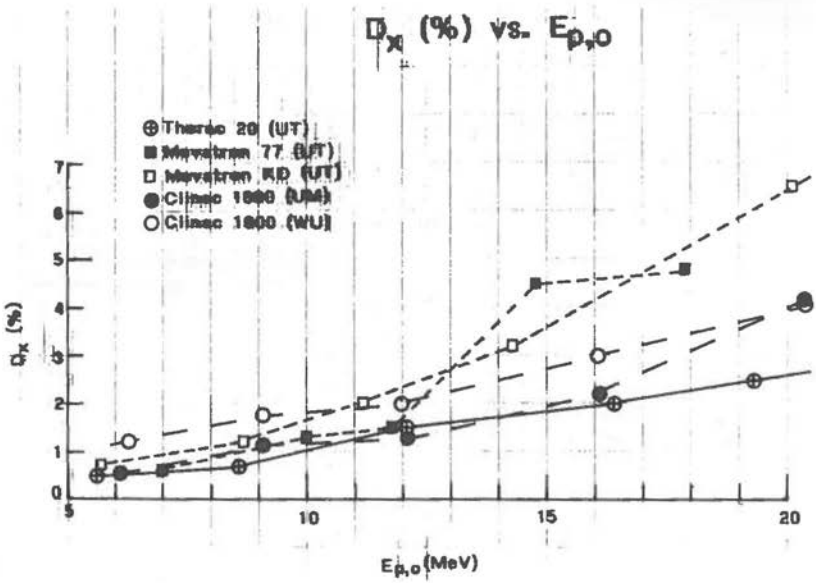

Figure 10. Comparison of bremsstrahlung dose, D_x, versus electron energy for all energies of the Therac 20, Mevatron, and Clinac radiotherapy accelerators (from NCI Working Group, 1989).

beam in the off-axis direction. They must rely on collimator scatter, which results in unusually high collimator leakage (Keys and Purdy, 1984; Pennington et al., 1988). From the above data, the NCI Working Group (1989) concluded that differences in depth-dose properties of the three types of machines were not clinically significant and that, through proper treatment planning, all machines were equally useful.

Electron beam depth dose exhibits a field-size dependence, as a result of the fact that all electrons reaching any point are scattered (cf. Fig. 5). Figure 11 illustrates the field-size dependence of square-field depth dose curves for a high and low electron beam energy. These data show the general trend towards increased surface dose, decreased therapeutic depth, and a shift towards the surface of R_{100} with decreasing field size. The decrease in therapeutic depth with decreasing field size is primarily due to lack of side-scatter equilibrium, previously discussed. In the commissioning of an electron therapy machine, one should measure square field depth-dose curves at intervals that permit the linear interpolation of other square field depth-dose curves within an accuracy of approximately 3%. This requires a higher frequency of measurement at the smaller field sizes, particularly at the higher electron beam energies. Electron square field sizes from 2x2 to 12x12 cm are usually sufficient for clinical use at energies below 25 MeV.

The depth-dose curve is approximately independent of how the field size was formed. For example, the depth-dose curve for an open 6x6-cm cone should be nearly the same as that for a 10x10-cm cone with a 6x6-cm cutout, even though the output at R_{100} may differ by a few percent. This may not be the case on radiotherapy accelerators that use a substantial amount of collimator scatter, e.g., Varian Clinacs. Therefore, at the time of commissioning an electron beam, one should check depth-dose curves to verify independence of how the field is constructed. If not independent, then the field size dependence of depth dose may have to be measured for each cone.

Rectangular field depth doses can be determined by the square root formalism. This formalism was first derived by Hogstrom et al. (1981) utilizing Fermi-Eyges scattering theory. It was shown that the depth dose for a rectangular field for length L and width W is given by

$$D^{L,W}(d) = [D^{L,L}(d) \cdot D^{W,W}(d)]^{1/2} \quad . \tag{3}$$

In applying this equation, one must realize that if one's convention is to normalize the maximum value of the depth-dose curve to 100%, then the resulting calculated depth-dose curve for the rectangular field must be normalized with its maximum to 100%. This will be necessary if R_{100} for the two square field sizes are not equal. In general, the equivalent square concept for rectangular electron fields does not work. Figure 12 compares the measured depth-dose curve for an elongated field with that calculated using both the square root method and the equivalent square method (4A/P, where A is area and P is perimeter). The equivalent square method overestimates the depth of penetration, whereas the square-root method precisely predicts the measured depth-dose curve. This formalism has been confirmed by Meyer et al. (1984) and Sharma and Wilson (1985). The square root formalism can also be used in the measurement of small square field central-axis depth-dose curves. It has been shown by Meyer et al. (1984) that the depth-dose for a small square field is given by

$$D^{W,W}(d) = \frac{[\, D^{L,W}(d) \,]^2}{D^{L,L}(d)} \quad . \tag{4}$$

Again, the resulting depth-dose curve must be normalized such that its maximum is 100%, if that is the convention adopted by your clinic. In the measurement of the depth-dose curve with a cylindrical ion chamber, the dimension of the active volume is usually greater in the dimension of the stem. Therefore, as illustrated in Fig. 13, the cylindrical ionization chamber should be oriented such that the stem is in the long dimension of the field for both depth-dose curve measurements. This serves two purposes: (1) it minimizes the dose gradient across the ionization chamber, and (2) it ensures a constant stem effect for both sets of measurements.

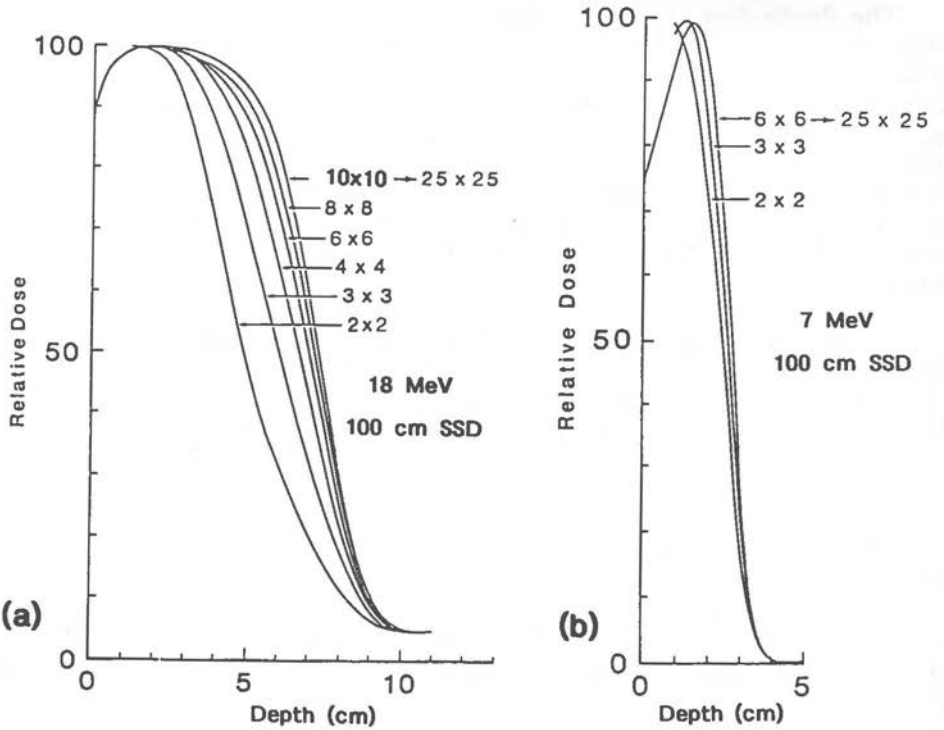

Figure 11. Depth-dose curves from the Mevatron 77 plotted for various field sizes at (a) 18 MeV and (b) 7 MeV (from Hogstrom and Meyer, 1984)

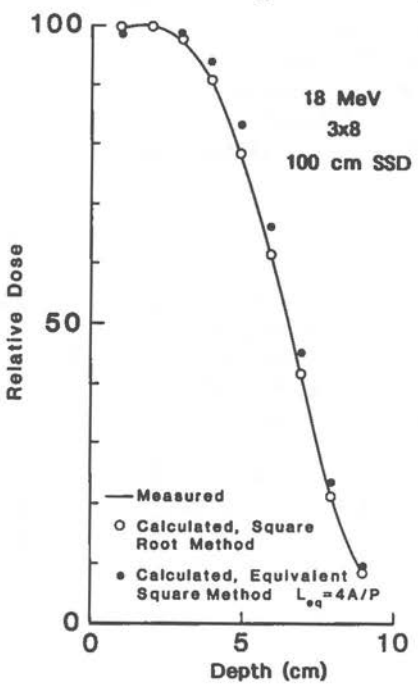

Figure 12. Comparison of measured depth dose with that calculated by the square-root method and by the equivalent square method for a 3x8-cm, 18-MeV beam on the Mevatron 77 (from Meyer et al., 1984).

B. Output Factor

Output is defined as the dose per monitor unit at a specified point in the electron beam. For rectangular, circular, or other symmetrical fields, output is measured on the axis of symmetry of the field (usually central axis). It is recommended that the depth of output measurement be at the depth of maximum dose, R_{100} . Although some define output at a constant depth, this practice is not encouraged because of the strong field-size dependence of depth dose, which can result in depth-dose factors that then exceed 110%. The output factor is defined as the ratio of output for a specified field to that of the reference field at the same energy and SSD.

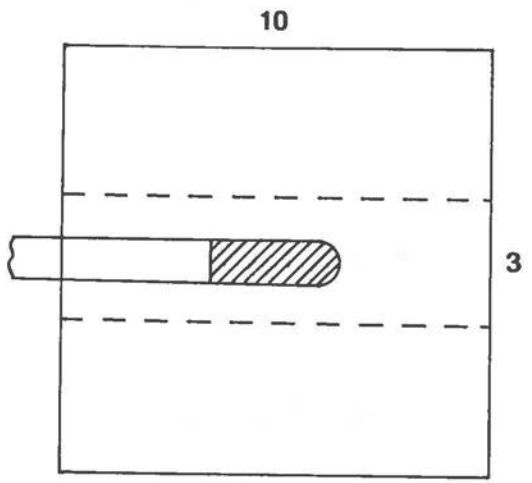

Figure 13. Orientation of cylindrical ionization for measurement of a 3x10 and 10x10-cm depth dose to be used in determining depth dose for a 3x3-cm field.

$$\%DD(3,3) = \frac{[\%DD(3,10)]^2}{\%DD(10,10)}$$

The output is a function of field size and depends strongly upon the method in which the field size is defined. There are four different components of collimation that may be used to create the patient's field, each which can influence the output factor; they are (1) the x-ray jaw settings, (2) the secondary collimation system, (cone, applicator, or trimmer bars), (3) lead or lead-alloy irregularly-shaped cutouts inserted into the secondary collimation system, and (4) skin collimation. In commercial electron radiotherapy machines, one of two fundamental collimation systems are used: the synchronous trimmer system or the treatment cone system.

The field size dependence of output arises because of electron scattering. Of most significance is the scattering of electrons in air and the loss of side-scatter equilibrium, which was previously described in Fig. 5 and predicts the output to decrease monotonically with decreasing field size. A secondary effect is due to scatter off edges or walls of the treatment

applicator. As a large field size is decreased, there is usually an increased probability of electrons scattering off the cones reaching central axis, which can result in a small increase in output with decreasing field size at intermediate field sizes until the previous phenomenon dominates.

1. Synchronous Trimmer System

In the synchronous trimmer system, the x-ray jaws and the trimmer bars are physically attached (e.g., AECL Therac 20, CGR Sagittaire, GE/CGR Saturne) or electronically attached (Mevatron, Hogstrom and Meyer, 1985) so that they track together, resulting in a continuously variable set of rectangular field sizes. Typically the field size defined by the x-ray jaws at isocenter is set 10 cm greater than that defined by the trimmer bars. The field size dependence of output is illustrated in Fig. 14 (Mills et al., 1982), where the output factor for the Therac 20 is plotted versus the side of square field at energies ranging from 6 to 17 MeV. In this system the output for rectangular fields depends upon which pair of jaws (upper or lower) produces the length and width. This is illustrated in Fig. 15 (Mills et al., 1985), where the output factor for Therac 20, 6-MeV beam is plotted for fields l0xX cm and Yxl0 cm, where X and Y are the two orthogonal dimensions of collimation. Again, using a Gaussian scatter model for pencil beams, it is possible to derive a formula that relates the output factor for rectangular fields with those of square fields. These are given by the following two equations:

$$OF(X,Y) = [OF(X,X) \cdot OF(Y,Y)]^{1/2} \qquad \text{(square-root method)} \qquad (5)$$

and

$$OF(X,Y) = [OF(X,Y_0) \cdot OF(X_0,Y)] + CF(X,Y) \text{ (1-dimensional method)}, \qquad (6)$$

where X_0 and Y_0 are reference field dimensions of 10 cm, and CF is a correction factor that accounts for differences primarily due to scatter off the x-ray jaws. Mills et al. (1985) have parameterized the correction factor by

$$CF(X,Y) = \begin{cases} 0, & \Delta \leq O \quad (7A) \\ C \cdot \Delta, & \Delta > O \quad , \quad (7B) \end{cases}$$

where

$$\Delta = \frac{(X-10)(Y-10)}{|\,(X-10)(Y-10)\,|^{1/2}} \quad . \qquad (8)$$

Equation (5), the square-root method, predicts rectangular output factors and is accurate within approximately 3%, being least accurate for large fields with large aspect ratios (e.g., 30xl0 cm). Equations (6)-(8), the 1-dimensional method, predict the output factor within 1.5% for rectangular field sizes ranging from 4x4 cm to 30x30 cm (Mills et al., 1985).

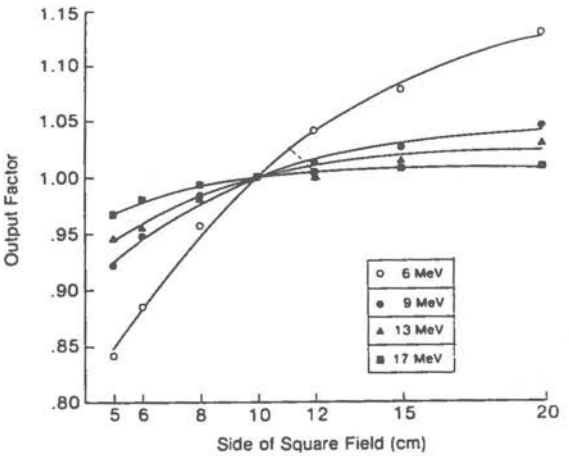

Figure 14. Plot of output factor versus side of square field for the 6,9,13, and 17-MeV electron beams of the Therac 20. The solid curves represent physical fits to the data based on scatter theory (from Mills et al., 1982).

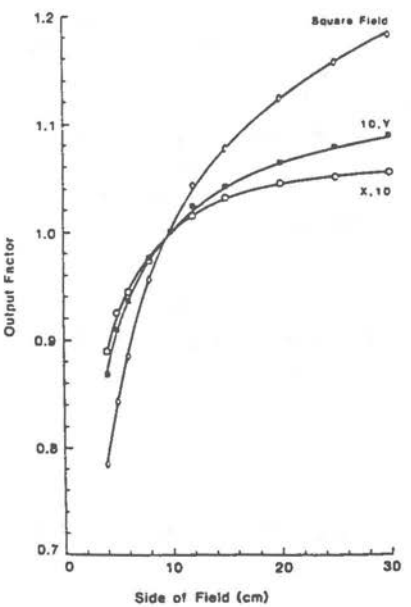

Figure 15. Plot of output factor versus side of field at 6 MeV on the Therac 20 for square fields (◊), rectangular fields 10xY (■), and rectangular fields Xx10 (0) (from Mills et al., 1985).

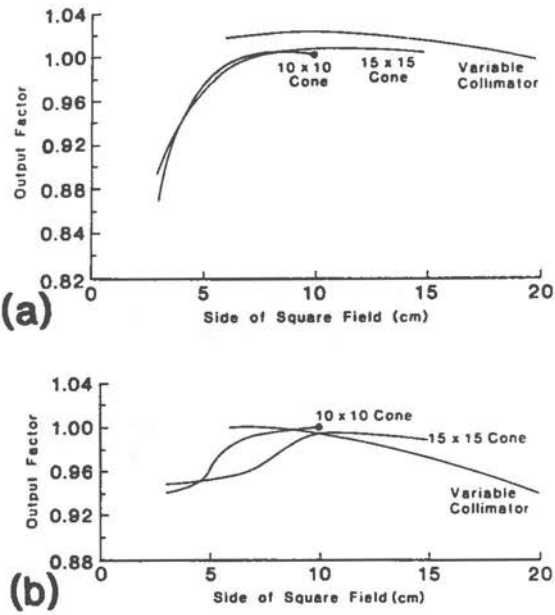

Figure 16. Dependence of output factors on side of square field for the 10-cm, 15-cm, and variable applicator of the Mevatron 77 at (a) 7 MeV and (b) 18 MeV (from Meyer et al., 1984).

2. Cone or Applicator System

In the machines employing cone or applicators for secondary collimation, the characterization of output factors is similar, but slightly different than above. First, there are only a few applicator sizes, which typically form a small number of square fields (e.g., 6-cm, 10-cm, 15-cm, 20-cm, 25-cm, and 30-cm square) and perhaps a few rectangular or circular fields. Rectangular fields are then formed by the use of cutouts that are inserted into the "open" cone, in which case the x-ray jaws remain set as opposed to tracking, as was the previous case. As pointed out by Biggs et al. (1979) and Mills et al. (1982), the output factor is influenced mostly by the x-ray jaw setting and to a lesser extent by the field size defined by an insert. The latter does become important for the smaller field sizes.

It is recommended that output measurements be made at each beam energy for all standard cone and insert combinations. The output factor for the cone (or applicator) size, C_s, with an insert size, I_s, is defined as

$$OF(E,C_s,I_s) = \frac{O(E,C_s,I_s)}{O(E,C_o,I_o)} \quad , \tag{9}$$

where C_o,I_o are the standard cone and insert used for calibration (typically 10x10-cm cone, with no secondary insert). This equation can be rewritten as

$$OF(E,C_s,I_s) = \left(\frac{O(E,C_s,I_0)}{O(E,C_0,I_0)}\right) \bullet \left(\frac{O(E,C_s,I_s)}{O(E,C_s,I_0)}\right) \quad , \tag{10}$$

where the first term is referred to as the open cone ratio and the second term as the blocking factor.

The output factor is usually stored at each energy, as either a table of values or a family of plots of output factor versus square field size for each cone. Figure 16 shows data for the Mevatron 77 (Meyer et al., 1984) at 7 MeV and 18 MeV. The output factor is often multiplied by the output of the reference field (typically 1 cGy per monitor unit) and stored as output.

It was shown by Biggs et al. (1979) that the output factor for rectangular and circular inserts could be estimated by an equivalent area concept. Although not specified in their paper, the equivalent area is often approximated by four times the area divided by the perimeter (4A/P). Biggs et al.'s data were limited to the energy range of 4-18 MeV and field dimensions greater than 4 cm; the calculated outputs were found to lie within 2% of measured data, provided no more than one-half of the open cone was blocked. For very small fields with dimensions less than 4 cm, this methodology may be less accurate and require more sophisticated calculational methods or direct measurement.

C. Off-Axis Dose Distribution

Off-axis dose distributions are typically expressed in one of two ways, off-axis ratios (OAR) or isodose distributions. The off-axis ratio is defined as the ratio of dose at a point off central axis to the dose at a point on central axis, where both points are the same depth from the surface of a water phantom. Off-axis ratios, when used to evaluate flatness, symmetry, and collimator leakage of the electron beam, are normally measured along the major axes of the beam and along diagonals for rectangular fields, at depths between the surface and R_{90}. Flatness and symmetry should be evaluated inside the beam's penumbra. For well-designed electron beams, off-axis ratios should lie within ±3% of the central-axis value along the major axes, and ±5% of the central-axis value along diagonals; this should be true for all energies and open cone sizes. Examination of the off-axis ratios in the umbral region indicates any electron leakage. For electron beams up to 20 MeV, leakage should be measured at or near the surface and should have values typically less than 2%. Values greater than 2% indicate possible leakage through the lateral confines of the electron beam collimation system.

Isodose curves are typically measured in a plane containing both the central beam axis and one of the major axes or in a plane perpendicular to central axis at a constant depth (referred to as beam's-eye-view (BEV) plane). For the former, it is recommended that the dose distribution be normalized such that 100% equals the maximum dose on central axis. Isodose values of 5%, 10%, 20%, . . . 70%, 80%, 90%, 95%, 100% and every

5% thereafter are recommended to be plotted.

Isodose distributions should be measured during machine commissioning for select square, circular, and rectangular field sizes. They should be measured in a plane defined by the central axis of the beam and one of the major transverse axes. Figure 17 shows such an isodose distribution for an open 10x10-cm, 15-MeV electron beam on a Siemens Mevatron 77. A study of this plot shows that the treatment volume (defined to be volume contained by 90% isodose contour) lies inside the geometric treatment volume (defined by projection of light field edges and depth of 90% dose). In treatment planning, it is important to realize that the treatment depth to the 90% isodose line does not extend to the R_{90} depth throughout the geometric field definition. As the edge of the light field is approached, one observes the 90% isodose line being pulled back such that there lies a region of decreased dose in the corners of the geometric treatment volume. A rule-of-thumb frequently used in treatment planning is that the light field extend 1 cm outside the lateral projection of the target volume; this can vary slightly with collimator design, beam geometry, and energy, but can be determined from measured isodose contours. If there is any doubt regarding coverage of the target volume by the 90% isodose contour, it is recommended that dose calculations be performed on a

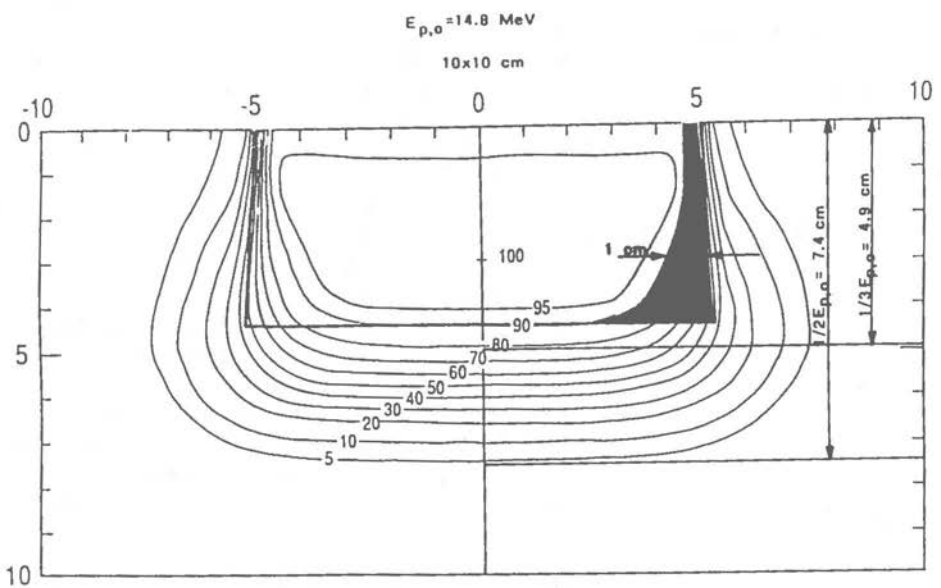

Figure 17. Isodose contours for 15-MeV electron beam of Mevatron 77 in a water phantom (redrawn from Meyer et al., 1984).

treatment planning computer. Measured isodose distributions then serve the following purposes:
(a) visualization of dose distributions for patient planning,
(b) input for hand-calculated or computer-calculated patient dose distributions,
(c) data to compare with dose distributions calculated by an algorithm on a treatment planning computer for verification of accuracy, and
(d) documentation of treatment beams for subsequent quality control or comparison with treatment beams of other accelerators.

D. Effects of Air Gap

Air gap plays a significant role in clinical electron beam dosimetry. As a result of beam divergence, an increased air gap results in a decreased dose and a corresponding broadening of the field. Also, there are modifications in the shape of the off-axis profiles of the beam, particularly in the penumbral region.

1. Virtual Point Source

The electron beam, exiting the vacuum window of a typical radiotherapy accelerator and bending magnet, is directed along the collimator axis and is a pencil beam having a small but finite radial and angular spread. In passing through the accelerator end window, scattering foils, beam monitoring transmission ionization chambers, intervening air, and any other materials in the beam, the electrons undergo multiple Coulomb scattering. At a downstream plane (e.g., level of beam-defining collimator), the electron beam is now broad but appears to have emanated from an electron source. ICRU (1984) defines an effective extended electron source, characterized by an effective position upstream of the plane, a mean square radius, and a mean square angular spread. This source, when placed in vacuum, would produce exactly the same distribution of the electron fluence in position and angle as the actual beam.

For the purpose of clinical dosimetry and treatment planning it is desirable to represent the extended electron source by a point source in vacuum so that divergence correction formulae such as the inverse square law can be applied. This point source is defined as the virtual point source (Schroder-Babo, 1983). The virtual point source is defined for a plane perpendicular to the central axis of the electron beam, which should be at the standard patient SSD (normally at the isocenter). It is defined as the point closest to intersecting the back projection of the mean directions of motion of electrons passing through pixels within the defined plane. The virtual point source is typically upstream from, but close to, the position of the effective extended electron source.

A number of methods for determination of virtual source position have been reviewed by Schroder-Babo (1983) and demonstrated by Jamshidi et al. (1986). Of those techniques reviewed by Schroder-Babo, the method whereby

off-axis beam profiles are measured in air several distances from the cone is recommended. In this method, the virtual source position is found by back-projection of the 50% width of the beam profiles obtained at these locations. A large field (20x20 cm) should be used in these measurements to minimize the collimator's influence and ensure side-scatter equilibrium. Field sizes greater than 20x20 cm should be used with caution, since it is important in this method that the electron fluence passing through the collimator be uniform. Figure 18 from Meyer et al. (1984) shows a set of measured off-axis beam profiles and the resulting determination of virtual source position. The virtual source position can also be determined by measuring the decrease in output as a function of distance. A plot of $1\sqrt{\text{reading}}$ versus position will also allow the determination of the virtual source position (Khan et al., 1978). Again, a large enough field must be used in these measurements to ensure side-scatter equilibrium; otherwise the results will falsely indicate that the source moves downstream (Jamshidi et al., 1986; Thomadsen et al., 1981; Meyer et al., 1984). Meyer et al. demonstrated this by comparing the measurement of source position using the two methodologies.

2. Characterization of Dose Output at Extended SSD

Central-axis dose output decreases with increasing air gap. This is a result of both beam divergence and electron scatter. Output will decrease according to inverse square from the virtual source position as a result of beam divergence. Output will also decrease because of scatter of electrons in air, which result in a loss of side-scatter equilibrium as discussed in

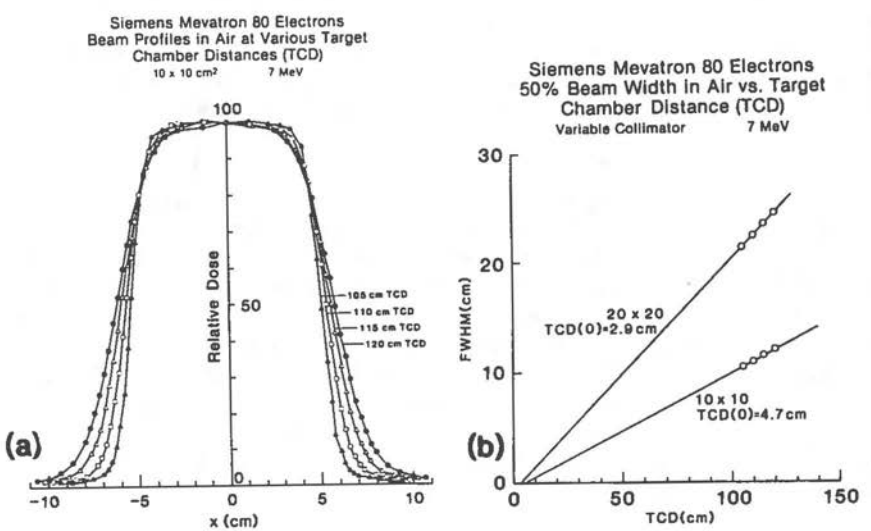

Figure 18. (a) Plot of in-air, off-axis profiles at various scattering target to chamber distances (TCD) for a 10x10-cm, 7-MeV electron beam on the Mevatron 77. (b) Plot of full width at half maximum (FWHM) versus TCD for data from (a) as well as for 20x20-cm

field. TCD (0) indicates virtual source position (from Meyer et al., 1984).

Fig. 5, being most significant for small field sizes and low energies. The contribution to dose from electrons scattered off the collimators also influences the output at extended treatment distances; output may either increase or decrease with air gap as a result of electron scatter, depending on collimator design, energy, field size, and air gap. The relationship between maximum dose at the extended SSD and the maximum dose at the nominal SSD is called the output correction. This ratio is characterized by the product of an inverse square factor from the virtual source position and an air gap correction factor, the latter accounting for the loss of side-scatter equilibrium and collimator scatter.

In the virtual SSD method, the dose output at the extended treatment distance is given by

$$O(E,I_s,SSD) = 0(E,I_s,SSD_0) \cdot \frac{(SSD_{vir}+R_{100})^2}{(SSD_{vir}+g+R_{100})^2} \bullet f_{air} \quad , \tag{11}$$

where $O(E,I_s, SSD_0)$ is the dose output at the standard, nominal source-surface distance (SSD_0), SSD_{vir} is the virtual source-surface distance for SSD_0, g is the excess air gap from SSD_0 ($SSD=SSD_0+g$), and f_{air} is defined to be the air gap correction factor. If the treatment field is rectangular, then from the work of Mills et al. (1982) it can be shown that a good estimate of f_{air} is

$$f_{air}\,(E,X,Y,g) = [f_{air}(E,X,X,g) \bullet (f_{air}(\,E,Y,Y,g)]^{1/2} \quad . \tag{12}$$

Meyer et al. (1984) have reported values of f_{air} for the Siemens Mevatron 77. The variation with field size of f_{air} versus g at 7 MeV and the variation with energy for a 6x6-cm field size are shown in Figs. 19(a) and (b), respectively.

Output at extended treatment distances has been parameterized by many clinics by absorbing the air gap correction factor into the inverse square factor, resulting in

$$O(E,I_s,SSD) = 0(E,I_s,SSD_0) \cdot \frac{(SSD_{eff}(E,I_s)+R_{100})^2}{(SSD_{eff}(E,I_s)+g+R_{100})^2} \quad , \tag{13}$$

where the air gap $g = SSD-SSD_0$, SSD_0 is the standard SSD (typically 100 cm), and SSD_{eff} is the effective SSD. As data of Deibel and Khan (unpublished) show, output versus SSD does not truly follow an inverse square dependence, particularly for low energy and small field size. This is due to loss of side-scatter equilibrium discussed in Fig. 5 and due to the collimator scatter. However, for air gaps of 10 cm and less, the output can be modeled by assuming the virtual source position moves as a function of

field size. Of course, the virtual source position does not actually move, since it is unaware when the field size changes. Therefore, an effective source position is defined as that source position which gives the best fit to the output-versus-air gap data, assuming inverse square falloff only.

Therefore, the effective source must be a function of field size, as determined for the Varian Clinac 1800 by Thomadsen et al. (1981) and Jamshidi et al. (1986). This method represents an alternative approach to the virtual SSD method; both are capable of predicting output at extended SSD. The effective method contains fewer physical principles in its formulation, and the multitude of source positions generated cannot be used in pencil-beam dose algorithms, which specifically model the lateral electron scatter in air.

3. Characterization of Depth Dose at Extended SSD

For most clinical conditions, the variation in percent depth doses at nominal and extended SSDs is clinically insignificant because of the finite penetration of the electrons less than 25 MeV. Khan et al. (1978) recommends multiplying the depth dose at the nominal SSD times a divergence factor (often referred to as the F-factor or Mayneord factor). For an extended SSD of 110 cm or less (normal SSD, 100 cm), application of the divergence correction factor to beams 25 MeV and less results in an increase in depth dose of less than 2%. Data from Hogstrom et al. (1984) demonstrate little difference for 15-MeV electrons or the Mevatron 77, as seen in Fig. 20.

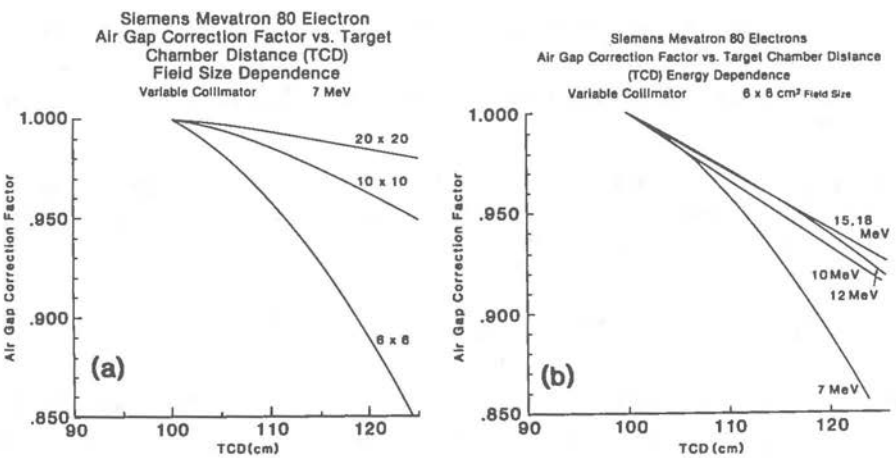

Figure 19. (a) Plot of air gap correction factors vs TCD (g = TCD-100 cm) for the 6x6, 10x10, and 20x20-cm field sizes at 7 MeV on the Mevatron 77. (b) Plot of air gap correction factor

versus TCD for the 6x6-cm field size at 7, 10, 12, 15, and 18 MeV (from Meyer et al., 1984).

On the other hand, there can be a significant difference in the depth dose at an extended SSD if there is substantial collimator scatter used to flatten the electron beam. This is the case for the Varian Clinac 1800; Fig. 21 compares the percent depth dose of the 6x6-cm open cone, 20-MeV beam at 100-cm and 110-cm SSD. Note how the decrease in scattered electrons for the 110-cm geometry results in a decrease in the surface dose, a more uniform depth dose, and a deeper R_{90}. In this case, it may be necessary to measure depth-dose curves at two SSDs.

4. Effects of Air Gap on Off-axis Dose Distribution

The off-axis ratio can vary significantly with air gap, particularly in the penumbra. The increase in air gap results in a significantly larger penumbra. At low energies (~6 MeV), the width of the penumbra (20%-80%) is approximately proportional to air gap. At higher energies (>14 MeV), the width of the penumbra near the surface is also approximately proportional to air gap, whereas at the deeper depths the penumbras are approximately equal (Fig. 20). Therefore, it is necessary to either calculate or measure the off-axis dose distributions or isodose contours at extended treatment distances.

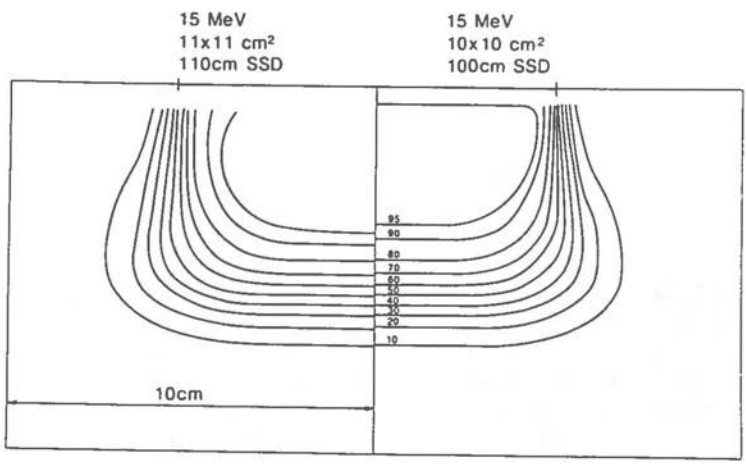

Figure 20. Comparison of isoionization curves at 100-cm and 110-cm SSD for a 10x10-cm, 15-MeV electron beam on the Mevatron 77 (from Hogstrom et al., 1984).

BEAM MODIFIERS AND TREATMENT PLANNING TOOLS

In preparation for electron-beam treatment, treatment planning tools are used to design a treatment scheme and the corresponding beam modifiers constructed, which uniformly irradiate the target volume while

protecting normal tissues both distal and lateral to the target volume.

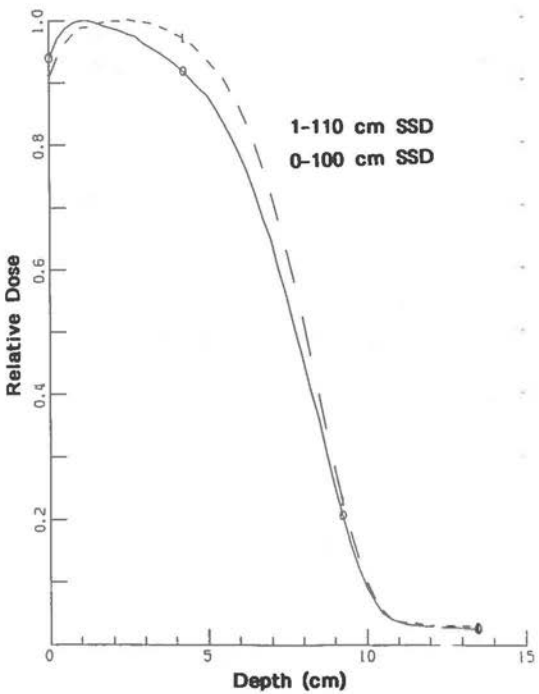

Figure 21. Comparison of depth dose at 100-cm and 110-cm SSD for a 6x6-cm, 20-MeV electron beam on the Varian Clinac 1800 (from NCI, 1989).

A. Blocking

In electron-beam therapy, thin lead or lead-alloy blocks are used to protect normal tissues and structures lateral to the target volume. It is necessary to know the block thickness and block extent required for proper blocking of electron beams. It is also imperative to understand the effects of blocking on beam output, depth dose, and penumbra.

1. Thickness of Lead Blocks

The required thickness of a lead block depends on the beam energy and the desired transmission through it. The transmitted dose varies with incident electron energy, primary bremsstrahlung dose, field size, and the gap between the patient and the collimator. For a particular machine and energy, the maximum transmission should occur when the collimation is in direct contact with the skin. The measurement of transmission of radiation through blocking material for a particular electron energy can be made with a plane parallel-plate ionization chamber in a phantom such as polystyrene. Transmission curves are obtained by plotting transmitted

ionization as a function of block thickness. Transmitted ionization is plotted as a percentage of maximum central-axis ionization in the absence of any lead shield. The measurement is made at the depth of maximum ionization, d_{max}. Shortly after adding even a very small thickness of lead, the depth of maximum ionization moves from its standard depth to close to the phantom surface (Khan et al., 1981). Therefore, the transmission curve should be measured with the parallel-plate chamber having its thin entrance window abutted to the downstream border of the lead shield. In Fig. 22, a transmission plot of ionization versus lead thickness is plotted for a variety of energies from the Sagittaire linear accelerator. From these data we can estimate a maximum range; beyond the maximum range few electrons are transmitted, the remaining dose being due to bremsstrahlung from the primary beam or bremsstrahlung generated in the lead shield as it stops the electrons. From the transmission curves one can estimate the minimum lead thickness required for shielding, as well as the level of bremsstrahlung dose for that particular shielding thickness. In Fig. 23, the lead thickness required to stop primary electrons is plotted as a function of the most probable incident electron energy. These data are taken from a CGR Sagittaire, an AECL Therac 20, a Siemens Mevatron 77 (Meyer et al., 1984), a Philips LMR-13 (Khan et al., 1981), and a Varian Clinac 1800 accelerator (Purdy et al., 1980). These data fall along a straight line defined by lead thickness in mm equaling one-half the incident electron energy in MeV. Because of the variation in thickness of thin rolled lead sheets, it is standard practice in our clinic to require an additional 1 mm of lead. Therefore, the thickness of lead shielding recommended for clinical use is given by:

$$t^{Pb}(mm) = 0.5 \bullet E_{p,o}(MeV) + 1 \quad . \tag{14}$$

If Lipowitz alloy (Cerrobend) is used, then its thickness will be 1.2 times that required for lead:

$$t^{Cerrobend}\,(mm) \;=\; 1.2 \bullet t^{Pb}\,(mm) \quad . \tag{15}$$

It is probably not necessary for individual measurements of transmission curves for each beam energy. Rather, shielding thickness can be selected based on the above equations. However, it is recommended that the physicist measure the broad beam transmission for those thicknesses of shielding to be used in the clinic. This is particularly important in the utilization of lead sheets for skin collimation, where normally as few sheets as necessary are used so that the weight of the lead shield lying on the patient is minimal. Lead shields are most frequently used in head and neck therapy and in chest wall treatment. Table I shows the data utilized for an accelerator at The University of Texas M. D. Anderson Cancer Center both for Cerrobend inserts and for lead collimation on the skin. The thicker amounts of lead (i.e., additional number of sheets) are often used over the eyes in order to minimize lens dose.

TABLE 1
Lead Blocking for Electrons on Therac 20

Collimator Inserts

Nominal Energy (MeV)	$E_{p,o}$ (MeV)	Insert Thickness (mm) Lead	Cerrobend	Skin Dose (%)
6	5.7	6.4 (1/4")	7.7	1
9	8.8	6.4 (1/4")	7.7	2
13	12.1	6.4 (1/4")	7.7	5
17	16.3	9.5 (3/8")	11.4	7
20	19.1	9.5 (3/8")	11.4	10

Skin Blocking

Nominal Energy (MeV)	$E_{p,o}$ (MeV)	Lead Skin Block* Thickness (mm)	Skin Dose (%)
6	5.7	1.6 (1x1/16")	7
		2.4 (3/32")	2
		3.2 (2x1/16")	1
9	8.8	3.2	6
		4.8 (3x1/16")	3
13	12.1	4.8	8
		6.4 (4x1/16")	5
17	16.3	6.4	11
		7.9 (5x1/16")	8
		9.5 (6x1/16")	7
20	19.1	9.5	10
		11.1 (7x1/16")	9

*selected as multiples of 1/16" stock for ease of fabrication

2. Skin Blocking

Skin blocking is a useful tool in electron-beam radiotherapy, primarily used (1) for maximum protection of critical structures and (2) for ensuring as uniform a dose distribution as possible within the field. Clinical indications for skin collimation are as follows: (1) small fields (particularly low electron energies), (2) protection of critical structures just outside the treatment field (e.g., eye), and (3) restoration of beam penumbra (e.g., extended treatment distances and arc electron therapy). The utility of skin collimation for small fields is illustrated in Fig. 24. In Fig. 24(a) we see the dose distribution for a 3x3-cm, 6-MeV electron field incident upon a patient at 100-cm SSD (air gap = 10 cm). Because of the low energy and 100-cm air gap, the beam penumbra is quite large; this coupled with the small field

size results in the dose distribution being essentially all penumbra. To improve the dose distribution, the first step is to enlarge the initial field to 5x5 cm and to add skin collimation to now redefine a 3x3-cm field. The dimensions of the skin collimation should be such that they intercept the penumbra of the larger field, with leakage outside the field being negligible and the dose inside the skin collimation being uniform. The resulting dose distribution, seen in Fig. 24(b), is more clinically useful than that of 24(a). This use of skin collimation is frequently used in treatment of small fields, such as eyelid tumors (Tapley, 1976), and treatment of the nose (Fields, 1986).

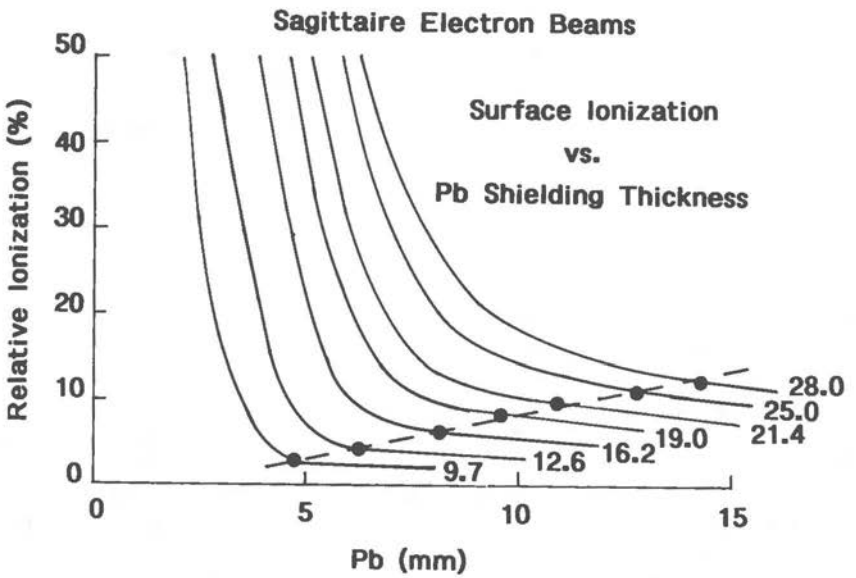

Figure 22. Plot of transmission curves (ionization versus Pb thickness) for multiple electron beams on the Sagittaire accelerator. Each curve is labeled by the most probable incident energy in MeV. The points demark the selected shielding thicknesses.

When skin collimation is used, it is important to know its effect on the dosimetry. Its effect on the penumbra is illustrated in Fig. 24. The field size dependence of depth dose is primarily due to scattering of electrons within the patient; therefore, the field size used for determination of depth dose should be that defined by the skin collimation, not that of the secondary collimator or trimmers. On the other hand, the field size dependence of dose output varies primarily with field size because of scattering of electrons in air so that output is reasonably estimated using the field size defined by the secondary collimator (trimmers, Cerrobend cutout, etc.), and neglecting the field size defined by the skin collimation.

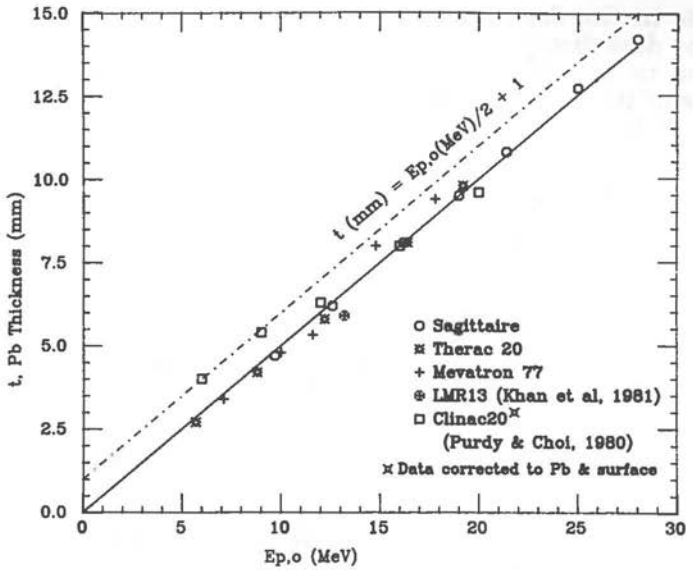

Figure 23. Plot of Pb thickness (selected to stop all primary electrons) versus the most probable incident electron energy for a variety of accelerators. The solid line indicates the Pb thicknesses recommended by AAPM Task Group 25 (Khan et al., 1991) and the dot-dashed line includes a 1-mm margin.

3. Internal Blocking

Internal lead shielding is often used in treatment of head and neck tumors for protection of the tongue and salivary glands (Tapley, 1976). Lead shielding cannot be placed directly in the oral cavity without protection from electron backscatter off lead. Electron backscatter is defined as the ratio of dose in the presence of the lead to that with the lead replaced by unit density tissue. It has been shown by Klevenhagen et al. (1982) that dose at a tissue-lead interface can be as much as 60% greater than that without the lead shield. They have shown that the electron backscatter factor is approximately related to the mean electron energy at the interface by

$$EBF = 1.0 + 0.735 \exp(-0.052 \bullet \bar{E}_z) \qquad (16)$$

where $\bar{E}$ is the mean energy in MeV of the electrons incident at the interface. The backscattered electrons are of much lower energy than those incident upon the interface and have a finite range. Transmission curves, from Lambert and Klevenhagen (1982), show the upstream penetration through unit density material of the backscattered electrons (Fig. 25).

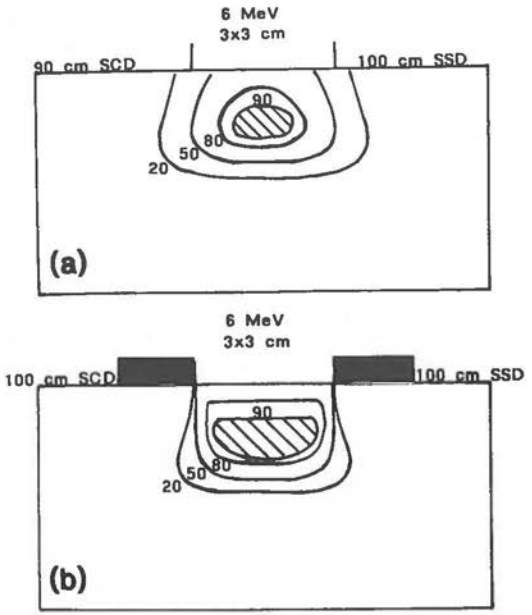

Figure 24. Selected isodose contours for a 3x3-cm, 6-MeV electron field: (a) field size defined by electron collimation 10 cm above water phantom; (b) field size defined by skin collimation with collimation upstream set to 5x5 cm. Highlighted area demonstrates increase in therapeutic volume (D>90%).

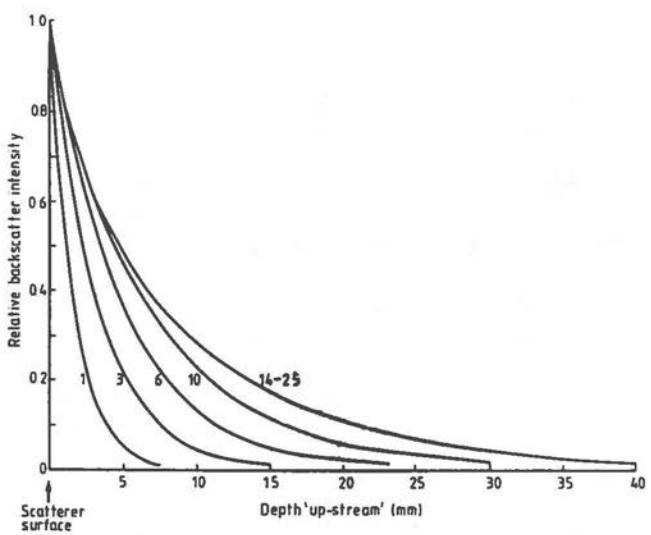

Figure 25. Plot of relative backscatter intensity versus depth upstream in polystyrene for various electron mean energies incident on lead (from Lambert and Klevenhagen, 1982).

Consider a 15-MeV electron beam incident laterally onto the cheek; the tongue at a depth of 3 cm is to be protected by lead shielding. What is the lead thickness and acrylic thickness required to protect the tongue and ensure that the electron backscatter factor (EBF) is less than 110%? The electron beam loses 2 MeV cm^{-1} resulting in 9-MeV electrons being incident on the tongue; therefore, in accordance with Eq. (14), 5.5 mm of

lead are required. From Eq. (16) the EBF is 1.46. From Fig. 25, 10 mm of polystyrene (equivalent to 9 mm of acrylic) are needed to reduce the 46% excess intensity by 78%, resulting in an EBF of 1.10. The 10 mm of polystyrene reduces the energy of the electron to 7 MeV, so that only 4.5 mm of lead is needed. The actual EBF is then 1.51 at the surface, and the 10-mm polystyrene reduces the EBF to 1.09.

B. Electron Bolus

Bolus is an essential component in the delivery of optimal electron-beam radiotherapy, as are compensators in photon-beam radiotherapy. Electron bolus is a specifically shaped material that is nearly tissue equivalent; it is normally placed either in direct contact with the patient's skin surface, close to the patient's skin surface, or inside a body cavity. This material is designed to provide extra scattering or energy degradation of the electron beam. Its purpose is to shape the dose distribution to conform to the target volume or to provide a more uniform dose inside the target volume.

Electron bolus in radiotherapy has three applications: (1) to increase dose to the patient's external surface, (2) to serve as a missing tissue compensator for surface irregularities and internal air cavities, and (3) to shape the coverage of the treatment volume to conform as closely as possible to the target volume while avoiding critical structures. In the latter two applications, bolus is being used to either eliminate or decrease the adverse effects of patient heterogeneities on the dose distribution, which can result in a geographical miss at depth, dose nonuniformity within the target volume, and excessive dose to distal critical structures.

There are various methods for increasing the surface dose to 90% in cases where it is less. The conventional method is to select a higher energy beam than required and to place a uniformly thick bolus to shift the depth of R_{90} to the depth of prescription, while increasing the surface dose to near 90%. The latter is accomplished as (1) surface dose of the higher energy electron beam is greater, and (2) the bolus places the skin at a deeper depth, further increasing the surface dose. This is the recommendation of ICRU (1984) and is the practice of our clinic.

For sloped surfaces, as are encountered in scalp irradiation, laying bolus on the surface is often undesirable and unnecessary because of the "self bolusing" caused by the sloping surface (Ekstrand and Dixon, 1982). Therefore, a method has been developed in which a polycarbonate plate is placed perpendicular to the beam and as close to the patient's surface as possible (Able, 1987). This method is also useful in postoperative patients with highly irregular surfaces. The polycarbonate plate, referred to as a scatter plate, serves as both an energy degrader and a scatterer to help irradiate irregular surfaces more uniformly. Skin collimation is normally used to restore the beam penumbra with such a technique. In the implementation of this technique, it is important that the light field be

large enough so that the electron fluence within the aperture defined by the skin collimator is uniform. Also, the outer edge of the skin collimation should extend sufficiently to shield the patient from the penumbra due to scattered electrons (Hogstrom and Meyer, 1984).

For clinical dosimetry usage, a table has been compiled that shows the surface dose, the depth in the patient to the proximal 90% depth dose, and the depth to the distal 90% depth dose, as a function of available bolus thicknesses. Table II is a portion of the table that has been developed for Mevatron KD data.

TABLE II

Acrylic Bolus Chart for Therac 20 Electron Beams
10x10-cm field at 100-cm SSD

PMMA* Thickness (in)	Water Equivalent Thickness (cm)	Skin Dose (%)	Depth to 90% (cm) Proximal	Distal
6 MeV				
0	0	67.6	0.72	1.60
1/8	0.37	78.5	0.35	1.23
3/16	0.55	84.3	0.17	1.05
1/4	0.73	90.5	0	0.87
9 MeV				
0	0	73.5	1.10	2.70
1/8	0.37	81.8	0.73	2.33
3/16	0.55	83.7	0.55	2.15
1/4	0.73	85.8	0.37	1.97
13 MeV				
0	0	81.5	0.45	3.98
1/8	0.37	89.2	0.08	3.61
3/16	0.55	90.6	---	3.43
1/4	0.73	91.4	---	3.25
17 MeV				
0	0	86.7	0.13	5.48
1/8	0.37	94.0	---	5.11
3/16	0.55	94.8	---	4.93
1/4	0.73	95.6	---	4.75
20 MeV				
0	0	88.2	0.05	6.31
1/8	0.37	96.2	---	5.94
3/16	0.55	96.8	---	5.76
1/4	0.73	97.3	---	5.58

*PMMA, polymethylmethacrylate

The absence of adjacent tissue in the direction perpendicular to the incident electron beam results in a decreased dose to tissues within the irradiated field. This phenomenon is of concern in the treatment of protruding target volumes, such as the nasal vestibule (Fields and Hogstrom, 1982; Fields, 1986, Hogstrom et al., 1983), particularly if the nasal septum is involved. Improved dose homogeneity is accomplished by placing bolus in the nasal cavity and surrounding the nose so that a very simple rule of thumb becomes evident -- that utilization of bolus to make the patient anatomy present itself more as a water phantom results in a more uniform dose distribution.

The most sophisticated utilization of bolus is to shape it such that the therapeutic isodose surface will closely encompass the irregular shape of the target volume and/or exclude critical structures from a dose that exceeds their tolerance. The two structures most frequently at risk in electron radiotherapy are the lung and spinal cord.

For constructing complex boli, a variety of methods have been utilized. Archambeau et al. (1981) have constructed shaped bolus by stacking wax strips over a portion of the patient's chest wall. Beach et al. (1981) achieved the same result by molding a rubber bolus to the skin surface and adjusting its thickness by using calipers to measure thickness and shaving to achieve the desired thickness. More promising methods utilize automatic milling machines. A technique for milling a mold into which beeswax is poured has been described by Andrew and McParland (1987), and a technique for milling of polyolephin wax has been described by Takizawa et al. (1987) and Smith et al. (1989).

In the clinical use of bolus, there are some basic principles that should be followed:

(1) Bolus should be nearly tissue equivalent, i.e., it should have a density and average atomic number near that of tissue. Obviously, water or saline solution is ideal if there is a method for containing their shape. A variety of solid bolus materials frequently used clinically and their properties are listed in Table III.

(2) Bolus should be placed either in direct contact with, or as close as possible to, the patient's skin surface. If the bolus is far from the skin surface (>2 cm), then it may be necessary to use skin collimation to restore the penumbra. It is sometimes desirable to restore the penumbra beneath a thick bolus even in contact with the skin.

(3) Bolus should have no sharp edges in the beam. A 90° edge results in a local hot/cold region of dose below the edge of the bolus. To prevent this from happening, there should be no 90° edges inside the treatment field when a field is partially bolused. Also, the outer edge of the bolus should extend outside the beam's penumbra. When inside the treatment field, the edge of the bolus should be tapered at least 45°, which reduces the hot/cold

volume of dose. A straight, 45° edge on a Superflab bolus can be cut using a paper cutter.

TABLE III

Electron Slab Bolus Material Properties

Material	Density	Flexible	Supplier
Slab Bolus Material			
Polymethyl-methacrylate	1.18	No	---
Polystyrene (clear)	1.04	No	---
Aquaplast	1.15	With heat	WFR/Aquaplast Corp. (Ramsey, NJ)
Moldable Bolus (wax base)	1.02	With heat	Radiation Products Design (Albertville, MN)
Superflab	1.02	Yes	Mick Radio Nuclear Inst. (Bronx, NY)
Elastomeric	1.03	Yes	Action Products (Hagerstown, MD)
Moldable Bolus Materials			
Water	1.0		---
Beeswax (yellow)	0.96		---
Paraffin	0.90-0.92		---
Silastic$_R$ Rubber	1.09		Dow Corning Co.
Superstuff (TX-151)	1.00		Oil Center Research, Inc. (Lafayette, LA)

(4) It is important that bolus intent be verified. Bolus intent can be verified in part by either computer calculations, in-vivo dosimetry, or phantom measurements. Calculations on a treatment planning computer can be performed by either inputting new patient contours that include bolus as part of the patient, or more preferably by obtaining a computed tomographic (CT) scan of the patient with the bolus in place.

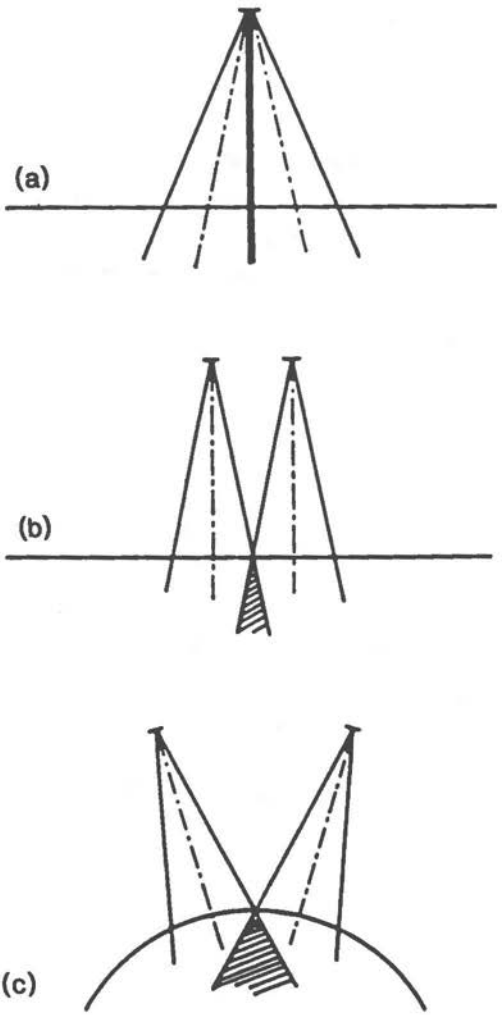

Figure 26. Three classifications of field abutment in order of increasing field overlap: (a) common source position, (b) parallel central axes, and (C) converging central axes (from ICRU, 1984).

C. Field Abutment

Another requirement in electron treatment is field abutment. Three examples of field abutment discussed in ICRU (1984) are illustrated in Fig. 26. Ideally, beams should be arranged such that their common edges coincide. If such is the case, then field abutment can produce a uniform dose, provided the penumbras of the abutted fields are identical and symmetrical about their match line. If the abutted fields have either unmatched penumbra, misaligned edges, or overlapped edges, then hot and cold spots occur. The magnitude of dose in these regions of

increased/decreased dose can be decreased by moving the abutment line two or three times during treatment. In electron irradiation of the spine, we create a broad penumbra by treating the patient at an extended SSD. If abutted electron fields are required to treat the spine, then the ideal technique of abutting broad, matched penumbra along a common edge is accomplished by a 90° couch and small gantry rotation, which places the electron source for the abutted field at the same point in space relative to the patient, as diagrammed in Fig. 26(a) (Maor et al., 1985; Meyer et al., 1984).

CLINICAL SPECIFICATIONS

A fixed electron beam is properly specified when the following information is provided:

1. Treatment machine
2. Nominal electron energy
3. Monitor unit rate
4. Source-to-skin distance (SSD)
5. Field shape
   a. Cone or trimmer setting
   b. Irregular field cutout
   c. Skin collimation
6. Bolus
7. Monitor units

From this information it is possible to calculate the dose delivered to a water phantom whose surface is at distance SSD.

Dose should be specified as the maximum dose to a muscle miniphantom located on central axis in a water phantom placed at the same SSD as that of the patient's; this is often referred to as the given dose. If the electron field is irregularly-shaped so that there is no axis of symmetry, then a central axis must be defined. In accordance with Shiu (1988), central axis should be that ray line passing from the virtual source through the maximum dose in a plane perpendicular to central axis (beam's-eye-view plane) at R_{100} of the open beam (irregular collimation removed). The number of monitor units necessary to deliver the given dose can be calculated using the dosimetry formalism described earlier in this paper.

Dose should be prescribed to the given dose, the 90% isodose contour, or some other isodose contour no less than 80%. The dose to the patient is related to dose in the water phantom. This relationship may be determined from a treatment planning dose computer or by manual methods. The method of calculation of patient dose should be specified on the calculation sheet, whether that be a computer isodose plan or a manual calculation. If the former, the computer printout should adequately specify the dose algorithm as well as associated beam parameters.

BIBLIOGRAPHY

AAPM (1983). American Association of Physicists in Medicine, RTC Task Group 21, "A protocol for the determination of absorbed dose from high-energy photon and electron beams," Med. Phys. 10, 741-771.

Able, C.M. (1987). "Evaluation of the MDAH total scalp electron irradiation technique," M.S. thesis, University of Texas Graduate School of Biomedical Sciences.

Andreo, P. and Brahme, A. (1983). "Fluence and absorbed dose in high energy electron beams," Acta Radiologica Supplementum 364, 25-33.

Andrew, J.W. and McParland, B.J. (1987). "An automated system for the production of bolus for electron beam treatments," p. 315-318 in The Use of Computers in Radiation Therapy, I.A.D. Bruinvis, P.H. van der Giessen, H.J. van Kleffens and F.W. Wittkämper, Eds. (Elsevier Science Publishers, Amsterdam).

Archambeau, J.O., Forell, B., Doria, R., Findley, D.O., Jurisch, R. and Jackson, R. (1981). "Use of variable thickness bolus to control electron beam penetration in chest wall irradiation," Int. J. Radiat. Oncol. Biol. Phys. 7, 835-842.

Beach, J.L., Coffey, C.W. and Wade, J.S. (1981). Individualized chest wall compensating bolus for electron irradiation following mastectomy: an ultrasound approach," Int. J. Radiat. Oncol. Biol. Phys. 7: 1607-1611 .

Biggs, P.J., Boyer, A.L. and Doppke, K.P. (1979). "Electron dosimetry of irregular fields on Clinac-18," Int. J. Radiat. Oncol. Biol. Phys. 5, 433-440.

Boag, J. (1972). "Surface ionization ratios for electrons in the energy range 3-11 MeV," Br. J. Radiol. 45, 229.

Bruinvis, I.A.D., Heukelom, S. and Mijnheer, B.J. (1985). "Comparison of ionization measurements in water and polystyrene for electron beam dosimetry," Phys. Med. Biol. 30, 1043-1053.

Ekstrand, K.E. and Dixon R.L. (1982). "The problem of obliquely incident beams in electron-beam treatment planning," Med. Phys. 9, 276-278.

Fields, R.S. (1986). "Mixed beam optimization techniques in head and neck radiotherapy," p. 15-36 in Proceedings of the First Annual Mevatron Users Conference (Siemens Medical Systems, Iselin, NJ).

Fields, R.S. and Hogstrom, K.R. (1982). "A computer model for combining electron and photon beams," p. 161-180 in Proceedings of the Electron Dosimetry and Arc Therapy Symposium B. Paliwal Ed., (Madison, American Institute of Physics, New York).

Hogstrom, K.R. and Leavitt, D. (1987). "Dosimetry of electron arc therapy," p 265-295 in Radiation Oncology Physics - 1986: Proceedings of the 1986 Summer School of the AAPM, H. Elson and C. Born Eds., (American Institute of Physics, New York).

Hogstrom, K.R., Mills, M.D. and Almond, P.R. (1981). "Electron beam dose calculations," Phys. Med. Biol. 26, 445-459.

Hogstrom, K.R., Mills, M.D., Meyer, J.A., Palta, J.R., Mellenberg, D.E., Meoz, R.T. and Fields, R.S. (1983). "Dosimetric evaluation of a pencil-beam algorithm for electrons employing a two-dimensional heterogeneity correction," Int. J. Rad. Oncol. Biol. Phys. 10, 561-569.

Hogstrom, K.R. and Meyer, J.A. (1984). "Electron beam characteristics of the Mevatron 77," p. 4 in Proceedings of the First Annual Mevatron Users Conference, (Siemens Medical Systems, Iselin, NJ).

Hogstrom, K.R. and Meyer, J.A. (1985). "Variable electron collimator for the Mevatron 77: design and dosimetry," p. 251 in Proceedings of the 1985 Mevatron Users Conference, (Siemens Medical Systems, Iselin, NJ).

ICRU (1984). International Commission on Radiation Units and Measurements, Radiation Dosimetry: Electron Beams with Energies Between 1 and 50 MeV, ICRU Report 35 (International Commission on Radiation Units and Measurement, Bethesda, Maryland).

Jamshidi, A., Kuchnir, F.T. and Reft, C.S. (1986). "Determination of the source position for the electron beams from a high-energy linear accelerator," Med. Phys. 13, 942-948.

Keys, R.A. and Purdy, J.A. (1984). "Radiation leakage from linac electron applicator assembly," Int. J. Rad. Oncol. Biol. Phys. 10, 713-721.

Khan, F.M., Doppke, K.P., Hogstrom, K.R., Kutcher, G.J., Nath, R., Prasad, S.C., Purdy, J.A., Rozenfeld, M. and Werner, B.L. (1991). "Clinical electron-beam dosimetry: Report of the AAPM radiation therapy committee task group 25," Med. Phys. 18, 73-109.

Khan, F.M., Sewchand, W. and Levitt, S.H. (1978). "Effect of air space on depth dose in electron beam therapy," Radiology 126, 249-252.

Khan, F.M., Werner, B.L. and Deibel, F.C. (1981). "Lead shielding for electrons," Med. Phys. 8, 712-713.

Klevenhagen, S.C., Lambert, G.D. and Arbari, A. (1982). "Backscattering in electron beam therapy for energies between 3 and 35 MeV," Phys. Med. Biol. 27, 363-373.

Lambert, G.D. and Klevenhagen, S.C. (1982). Penetration of backscattered electrons in polystyrene for energies between 1 and 25 MeV," Phys. Med. Biol. 27, 721-725.

Maor, M.H., Fields, R.S., Hogstrom, K.R. and Van Eys, J. (1985). "Improving the therapeutic ratio of craniospinal irradiation in medulloblastoma," Int. J. Radiat. Oncol. Biol. Phys. 11, 687-707.

Meyer, J.A., Palta, J.R. and Hogstrom, K.R. (1984). "Demonstration of relatively new electron dosimetry measurement techniques on the Mevatron 80," Med. Phys. 11, 670-677.

Meyer, J.A., Hogstrom, K.R., Fields, R.S. and Maor, M.H. (1984). "Treatment planning using CT for combined electron-photon irradiation of the craniospinal axis," Med. Phys. 11, 409.

Mills, M.D., Hogstrom, K.R. and Fields, R.S. (1985). "Determination of electron beam output factors for a 20-MeV linear accelerator," Med. Phys. 12, 473-476.

Mills, M.D., Hogstrom, K.R. and Almond, P.R. (1982). "Prediction of electron beam output factors," Med. Phys. 9, 60-68.

NCI Working Group (1989). "Evaluation of high energy electron external beam treatment planning (1986-1989)," Univ. Michigan Medical Center, Univ. of Texas M.D. Anderson Cancer Center, Washington University Mallinckrodt Institute of Radiology, private communication.

Pennington, E.C., Jani, S.K. and Wen, B.C. (1988). "Leakage from electron applicators on a medical accelerator," Med. Phys. 15, 763-765.

Purdy, J.A., Choi, M.C. and Feldman, A. (1980). "Lipowitz metal shielding thickness for dose reduction of 6-20 MeV electrons, " Med. Phys. 7, 251-253.

Schröder-Babo, P. (1983). "Determination of the virtual electron source of a betatron," Acta Radiologica Supplementum 364, 7-10.

Sharma, S.C. and Wilson, D.L. (1985). "Depth dose characteristics of elongated fields for electron beams from a 20 MeV accelerator," Med. Phys. 12, 419-423.

Shiu, A.S. (1988). "Three dimensional electron beam dose calculations," Ph.D. dissertation, University of Texas Graduate School of Biomedical Sciences.

Smith, R.M., Galvin, J.M., Needham, M. and Smith, A.R. (1989). "Computer aided design and fabrication of electron compensation bolus," Med. Phys. 16, 455.

Takizawa, M., Sone, S., Watanabe, T., Imai, Y., Imai, S. and Miyazawa, M. (1987). "An interactive desk-top compensating filter maker using Compact -3D NC-mill," p. 307-310 in The Use of Computers in Radiation Therapy, I.A.D. Bruinvis, P.H. van der Giessen, H.J. van Kleffens and F.W. Wittkämper, Eds. (Elsevier Science Publishers, Amsterdam).

Tapley, N. (1976). Clinical Applications of the Electron Beam, Tapley, N duV., Ed. (John Wiley and Sons, New York).

Thomadsen, B.R., Asp, L.W., van de Geijn, L., Paliwal, B.R. and Po Cheng, C. (1981). "Perturbation of electron beam doses as a function of SSD due to the use of shielding blocks on the Clinac-18," Med. Phys. 8, 507-509.